

# Characterization of Orbital Debris Attributes Using Functional Data Analysis

Emily Gerber, Thomas Kelecy<sup>1</sup>, and Jason Balke

*L3Harris, Colorado Springs, CO USA*

[Emily.Gerber@L3Harris.com](mailto:Emily.Gerber@L3Harris.com), [Thomas.Kelecy@L3Harris.com](mailto:Thomas.Kelecy@L3Harris.com), and [Jason.Balke@L3Harris.com](mailto:Jason.Balke@L3Harris.com)

## ABSTRACT

The value of techniques which might provide a more relevant characterization, and hence improved information on dynamic and physical attributes of non-resolved debris objects, will support improved attribution and custody of the increasing population of orbital debris. Previous work has proposed a taxonomical approach to characterizing orbital debris [1]. Others have proposed characterization techniques which move away from using time and frequency domain analyses of photometric data samples using information theoretic and functional data analysis (FDA). This approach showed some success in characterizing the physical and dynamic attributes of space objects from non-resolved photometric observations [2, 3]. Though promising, the results also revealed shortcomings where ambiguous characterization of the states resulted due to limited information content when only photometric data were available. Subsequent work [4] demonstrated a remarkable reduction in the ambiguity of characterized states when multiple data types were combined in the characterization step of the FDA process. Inclusion of photometric, tracking, Long Wave Infra-Red (LWIR) and Radio Frequency (RF) measurement types resulted in very reliable characterization of active, passive, dormant and transitioning satellite states.

Other recent research has also demonstrated the viability of collecting spectroscopic measurements to support orbital debris characterization [5]. In this work we continue along taxonomical lines and apply the FDA approach to characterizing orbital debris attributes that include simulated photometric, dynamic, thermal and spectroscopic attributes to selected classes of debris which include a tumbling rocket-body, defunct (uncontrolled) satellites of different types, and “typical” debris parts such as solar panel material, Multi-Layer Insulation (MLI), aluminum panels, etc. Simulated spectroscopic measurements will also be included in the FDA characterization to evaluate the value of including that data type in the FDA characterization. The analysis will then be extended to include actual photometric and astrometric data on active and passive satellites. Additional characterization techniques will be explored and discussed for the different measurement phenomena. Information gain in the characterization when including specific combinations of measurement and analysis types are explored.

**Keywords:** Orbital Debris Characterization; Probabilistic Analysis; Information Theory; Classification; Multi-Spectral.

**Declarations:** none

**Funding:** none

**Conflicts of interest/Competing interests:** none

**Availability of data and material:** none

**Code availability:** none

## 1. INTRODUCTION

Orbital debris objects can be observed from Earth or space-based sensors using different sensor modalities to try and learn information about the object. Fusion of multiple data types, like astrometric, photometric, thermal, Radio Frequency, and Albedo-Area Product have been used to characterize objects. The combination of the different measurement modalities allows for unambiguous characterization of different classes of satellites [1]. Now, is there a single measurement type that can be used to uniquely classify different types of debris objects? Multi-spectral measurements, taken over a series of wavelengths, have the potential to unambiguously classify different debris

---

<sup>1</sup> Now with the Stratagem Group

objects. Multi-spectral measurements give insight into the different material and reflective properties unique to an object. By looking at the measurements across the spectrum, a debris object can be fingerprinted. With this fingerprint, the object can be uniquely classified based on the multi-spectral measurements. This paper looks at the effectiveness of creating the fingerprint of six (6) different debris objects with a set of training data and the ability to match the fingerprint with a set of test data. The objects of interest are TDRS, DirecTV-2, a rocket body, solar panel, multi-layer insulation (MLI), and an aluminum sheet.

The two main goals of this paper are to (1) Evaluate the ability to unambiguously classify different debris objects using multi-spectral measurements and (2) Look at the methods for characterizing the simulated data and how well they apply to real data. Other important aspects addressed in this paper are the assumptions made in the modelling of the training and testing data of the debris objects and the decisions behind the quantity of training and testing data along with the parameters used for characterization.

The paper is organized as follows. Section 2 describes the problem formulation. Section 3 describes the simulation setup and the generation of the sample observational data. Section 4 describes the functional approach where each measurement is modelled as a series expansion that can be analyzed for information content. In section 5 the analysis for determining the debris classification using multi-spectral measurements is presented. Section 6 describes the same analysis processed used on real photometric data. Section 7 provides conclusions on the viability of using the proposed techniques to classify object attributes.

## 2. PROBLEM STATEMENT AND ASSUMPTIONS

A debris object can be classified using characterization techniques of the physical attributes of the object. The hypothesis in this work evaluates how well multi-spectral measurements can uniquely classify debris objects. Multi-spectral measurements taken from a ground-based observatory can provide insight into the different material properties of an object. Whereas photometric, astrometric, and Albedo-Area Product measurements of the different objects could lead to ambiguities. Debris objects with a similar size and rotation rate could produce similar light curves and that would be difficult to uniquely distinguish. Same with debris objects in similar orbits would have the similar dynamic attributes that would not allow for unambiguous characterization. The use of multi-spectral measurements over a series of wavelengths can provided enough information about an object to uniquely classify it.

Analysis was performed on six (6) object models, the DirecTV-2 satellite, Figure 1, TDRS-10 satellite, Figure 2, a Centaur rocket body, Figure 3, a solar panel, a sheet of multi-layer insulation (MLI), Figure 4, and an aluminum sheet. The TDRS and DirecTV satellites were modeled as milled aluminum boxes, with silicon solar panels and Astroquartz fabric antennas. The rocket body was modeled as a cylinder, and the reflective surfaces of the cylinder were modeled as 180 facets, with each facet joined together every  $2^\circ$  about the cylinder's circumference. The surface of the rocket body was assumed to be black anodized aluminum. The solar panel is the same dimensions as the DirecTV-2 solar panel and with surfaces modeled after the sun side and shade side of solar cells. The MLI object was modeled with the lower half of the object twice as dense as the upper half. This allowed the center of mass to be offset from the center of pressure, enabling solar radiation pressure to enact a greater torque on the debris objects to induce rotation. The aluminum sheet is a 5 ft by 3 ft panel made of polished aluminum.



Figure 1. DirecTV-2 satellite (Boeing 601 bus)

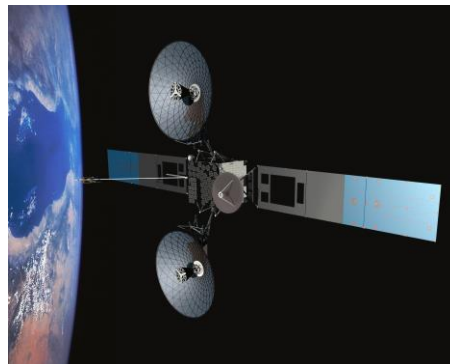


Figure 2. TDRS 10 satellite (Boeing 601 bus)



Figure 3. Centaur Rocket Body

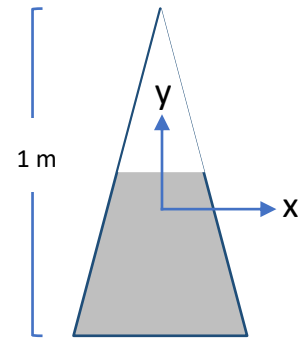


Figure 4. Simulated MLI Debris

For the debris objects being examined, the feature parameters are physically constrained by known material properties, sizes, shapes, the physics associated with the dynamics. One observation pass is considered to be one observation sample. As the result of differing observation geometries exposing different surfaces at different orientations over different observing passes, multi-spectral signature samples can look quite different from pass to pass. Examples of this are presented in the next section. It is assumed that the problem as stated is observable – the characteristic attributes can be extracted given a sufficiently large number of samples.

Given:

- Models of debris objects: TDRS, DirecTV-2, rocket body, solar panel, MLI, and aluminum sheet.
- Multiple parameter signature models for: multi-spectral measurements, astrometric tracking, photometric, and albedo-area-product.
- The physical/numerical constraints on these parameters.
- Gaussian statistical noise of the measurements (multi-spectral, astrometric, photometric, and albedo-area-product).
- Sufficiently large sample sets of each measurement type to derive statistics indicative of a class of debris object as derived from the model parameters.

Determine:

- Parameterization models that capture the essential physical attributes from the observation types (polynomial and Fast-Fourier Transform).
- Probabilistic metrics that provide a measure for how likely one or more of a given measurement types is to be associated with an ensemble population of representative measurement metrics associated to a given debris object as inferred from model parameter statistics derived from independent sets of measurements.

### 3. SIMULATED CASES

Multi-spectral, astrometric, photometric, and albedo-area product measurements were simulated for all six of the debris objects. The measurements were simulated with a hypothesized sensor located on Cyprus (e.g. the Starbrook sensor located at Geodetic Latitude =  $34.91278^\circ$  N, Longitude =  $32.88389^\circ$  E, Geodetic Altitude = 1773 m). Measurements were only taken when the object was visible to the sensor, the sun was illuminating the object, and the ground site was in darkness. Each set of measurements were taken over fifteen (15) minute intervals with five (5) second cadences.

In order to generate enough testing and training data for the functional data analysis, the simulations were run in a Monte Carlo like fashion. For each debris object and measurement type, a minimum of 250 Monte Carlo runs were completed. A single Monte Carlo run counted as an individual measurement set to be characterized. Each of the runs varied the initial epoch uniformly over a year to account for seasonal variations, the initial orbit parameters to account for common orbits in Geosynchronous (GEO) orbits, and the rotation rate of the object was Gaussian distributed based on a mean and sigma from steady-state analysis of debris objects.

To better understand the behavior of a tumbling debris object, the orbit and attitude dynamics were simulated using numeric integration over the course of one year. The simulation used various initial attitudes and body rates, and

accounted for Earth gravity perturbations up to J6, third body effects from the Moon and Sun and external torques from gravity gradient and solar radiation pressure. It was expected that when attitude dynamics of the objects were simulated, they would eventually reach a steady state of rotation. This steady state rotation could then be used in the generation of multispectral data, to avoid computationally expensive numeric simulation. When the dynamics were simulated over the course of one year it was found that the MLI debris object would typically reach a steady state of rotation of  $\sim 2^\circ/\text{s}$  about its x or y axis.

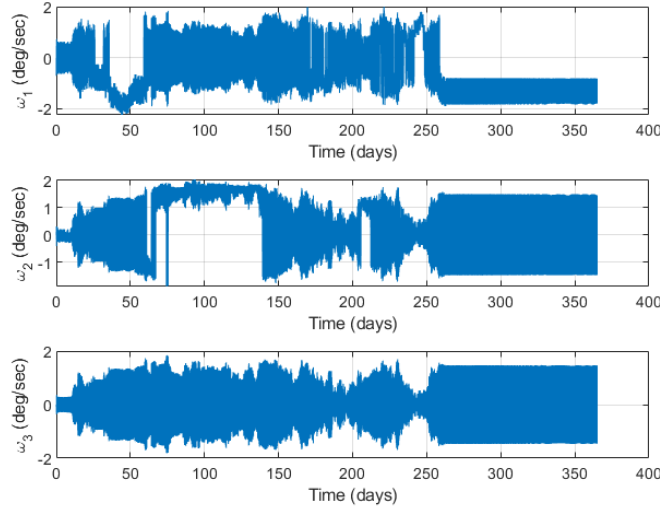


Figure 5. Simulated Body Rate Data of the MLI Object

This steady-state result along with similar simulations of the other debris objects gave steady-state rotation rates to be used in the Monte Carlo simulations. After more research, an additional set of 250 Monte Carlo measurement sets per degree object was simulated where each object had an initial rotation rate of zero (0) rad/sec. This was to focus on the physical material properties signatures from the multi-spectral measurements and not the dynamic rotation signatures.

### Simulated Multi-Spectral Measurements

The multi-sepctral measurement model is a function of both time and wavelength. As described in detail by Hall et al. [16], multi-spectral observations can be modeled by assuming a “wire-frame” model that provides orientation and area of each facet of each of each physical component of the debris being modeled. In particular, the  $k^{\text{th}}$  facet of the  $j^{\text{th}}$  component is characterized by its surface area  $A_{j,k}$  and normal unit vector,  $\mathbf{n}_{j,k}$ . The facets are typically defined in the body frame but, if associated with an articulating component, could vary with time. The spectral intensity (or spectral radiance),  $L$ , of sunlight reflected from the entire debris object has units of  $\text{W ster}^{-1} \mu\text{m}^{-1}$ . It is a function of time and wavelength and is modeled as a composite summation of all components visible to the sensor:

$$L(t, \lambda) = F_{sun}(t, \lambda) \left\{ \sum_{j,k} A_{j,k} \langle \mathbf{n}_{j,k} \cdot \mathbf{o} \rangle \langle \mathbf{n}_{j,k} \cdot \mathbf{s} \rangle \rho_j(\lambda, \mathbf{n}_k, \mathbf{o}, \mathbf{s}) \Psi_{j,k}(\mathbf{o}, \mathbf{s}) \right\} \quad (1)$$

where  $F_{sun}(t, \lambda)$  denotes the illuminating solar irradiance ( $\text{W ster}^{-1} \mu\text{m}^{-1}$ ),  $\mathbf{o}$  and  $\mathbf{s}$  denote the time -dependent debris-to-observer and debris-to-sun unit vectors, and the function  $\rho_j(\lambda, \mathbf{n}, \mathbf{o}, \mathbf{s})$  denotes the surface material bidirectional reflectance distribution function (BRDF) for component  $j$ .

The material composition formulation assumes that the surfaces of each debris object component can be modeled as a mixed set of distinct materials compiled from a BRDF database [17]. With this assumption the effective BRDF for the  $k^{\text{th}}$  facet of the  $j^{\text{th}}$  debris component may be written as a sum over the individual material BRDF’s as follows:

$$\rho_j(\lambda, \mathbf{n}_k, \mathbf{o}, \mathbf{s}) = \sum_m f_{j,m} \beta_m(\lambda, \mathbf{n}_{j,k}, \mathbf{o}, \mathbf{s}) \quad (2)$$

where  $f_{j,m}$  denotes the fractional area of component  $j$  covered by material  $m$ , and  $\beta_m(\lambda, \mathbf{n}, \mathbf{o}, \mathbf{s})$  denotes the pre-tabulated, laboratory-measured BRDF for the material  $m$ . Equation (2) is computed using a materials database and substituted into equation (1) based on the surface-sun-observer geometry and debris object attitude.

### Simulated Photometric Measurements

The simulated photometric measurements were modelled as a function of the physical characteristics of the debris objects, the position of the object, observation site, and sun using a Cook-Torrance BRDF model. The solar panels on the satellite objects are assumed to be facing the sun directly. The reflectivity of the entire object was determined through the combination of the facets illuminated by the sun and visible to the observer. The reflectivity of the components of the objects was a combination of the diffuse and specular reflection components.

$$Reflectivity = SurfaceArea * (N \cdot r_{sun}^{body}) * (N \cdot r_{obs}^{body}) * (Ref_{diffuse} + Ref_{specular}) \quad (3)$$

Where  $N$  is the surface normal vector and the dot product with the sun body unit vector and the observer body unit vector. The diffuse and specular components are dependent on the associated material coefficients. This reflectivity calculation is repeated for all of the illuminated and visible surfaces of the debris object. The reflectivity is then used to determine the visual magnitude of the object.

$$visualMagnitude = mag_{sun} - 2.5 \log \left( \frac{Reflectivity}{r_{obs}^2} \right) \quad (4)$$

Where  $mag_{sun} = -27.26$ , the r-band stellar magnitude.  $r_{obs}$  is the distance from the observer to the object. The visual magnitude of the satellite is calculated at each time step and has a  $1 - \sigma$  noise applied of 0.18 Mv. The simulation of the photometric measurements follows the same calculation for all debris object models, but the attitude, physical characteristics, and position of the debris objects produce unique results that are used in the analysis for object characterization.

### Simulated Tracking Measurements

To simulate the tracking measurements, first the Right Ascension and Declination were found at all of the individual timesteps. The Right Ascension and Declination measurements are the simulated astrometric products of an optical sensor image of the satellite. The optical measurements are only recorded when the debris object is illuminated by the sun and the ground observation site (Starbrook Sensor) is in darkness. The measurements are a function of the dynamics of the system, specifically the position of the satellite and the observation site.

### Simulated Emissivity-Area-Product Measurements

The simulated emissivity-area-product measurements are a product of LWIR measurements of a debris object. It is a function of the thermal radiation and the projected area of the object. Skinner, et al. describe the emissivity-area-product as the ratio of the gray body thermal radiation to the black body thermal radiation times the projected area of the object. In other words, it is a measure of the self-emitting thermal signature of an object, which can be used to characterize an object [4, 5, 6, 7]. Similar to the simulated photometric measurements, only the components of the object that are illuminated by the sun and visible to the observer were considered. The emissivity-area-product can be determined by the following equation:

$$EAP_{surface} = SurfaceEmissivityCoefficient * SurfaceArea * (N \cdot r_{obs}^{body}) \quad (5)$$

The emissivity-area-product is calculated for all of the observable surfaces and the sum of the emissivity-area-products of all the surfaces equals the total emissivity-area-product of the object. The emissivity-area-product is calculated at each timestep and has a  $1 - \sigma$  noise of 0.5 m<sup>2</sup> applied. For each of the characterization states, the emissivity-area-product was calculated using the above equations. Similar to the photometric measurements, the emissivity-area-product gives insight to the stability of the object for object characterization.

Below shows simulated measurements of the different debris objects with a Gaussian distributed rotation rate.

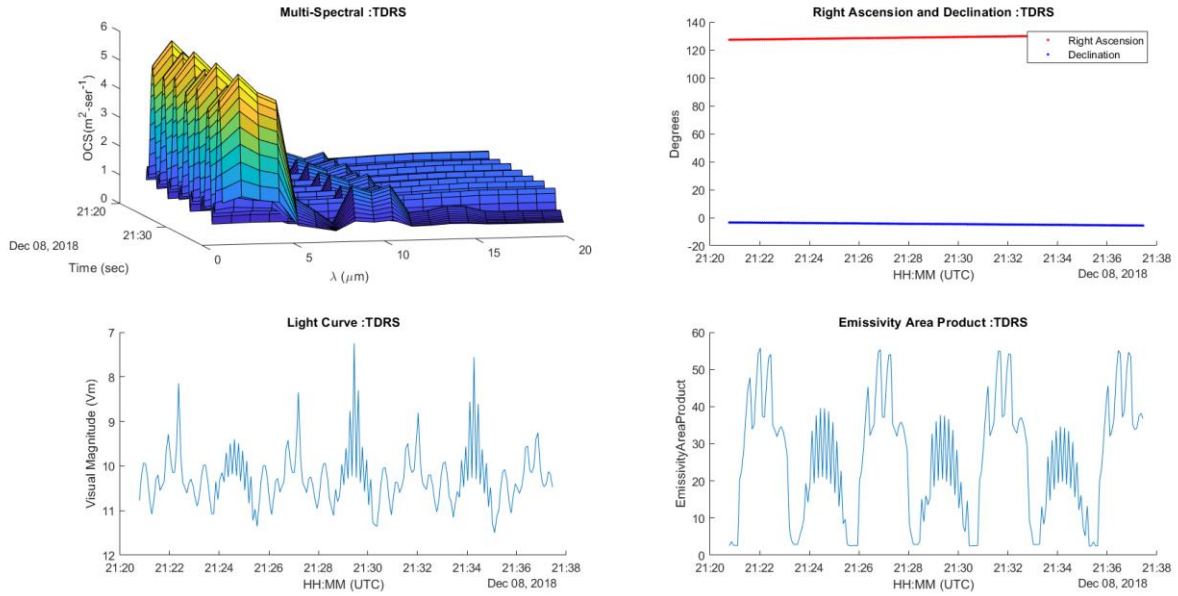


Figure 6. Simulated Measurements : TDRS

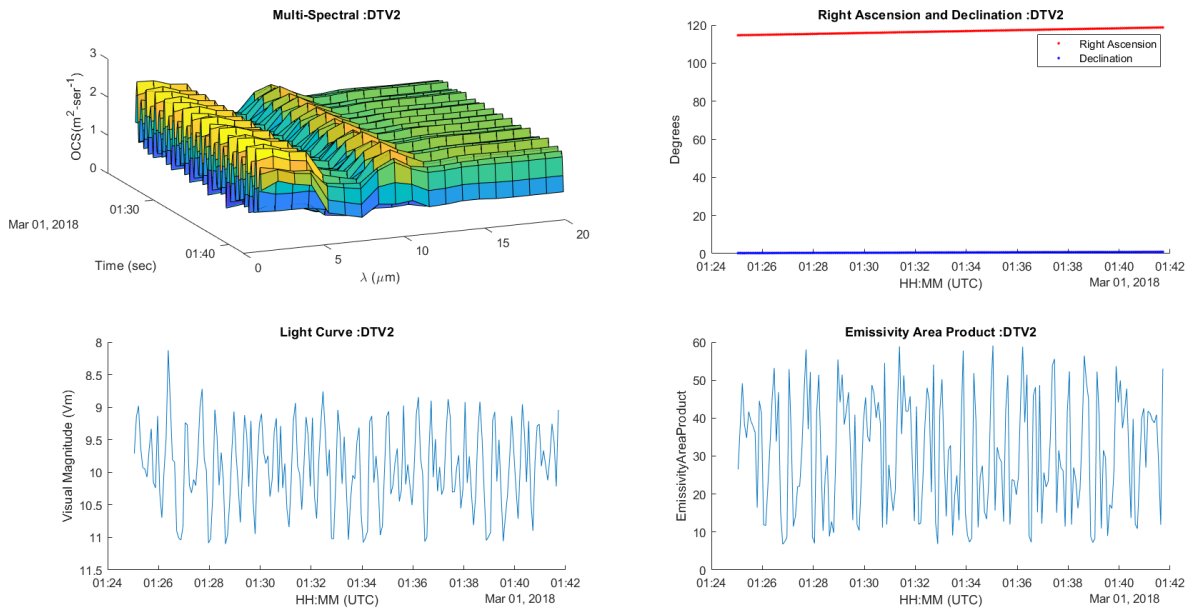


Figure 7. Simulated Measurements : DirecTV-2

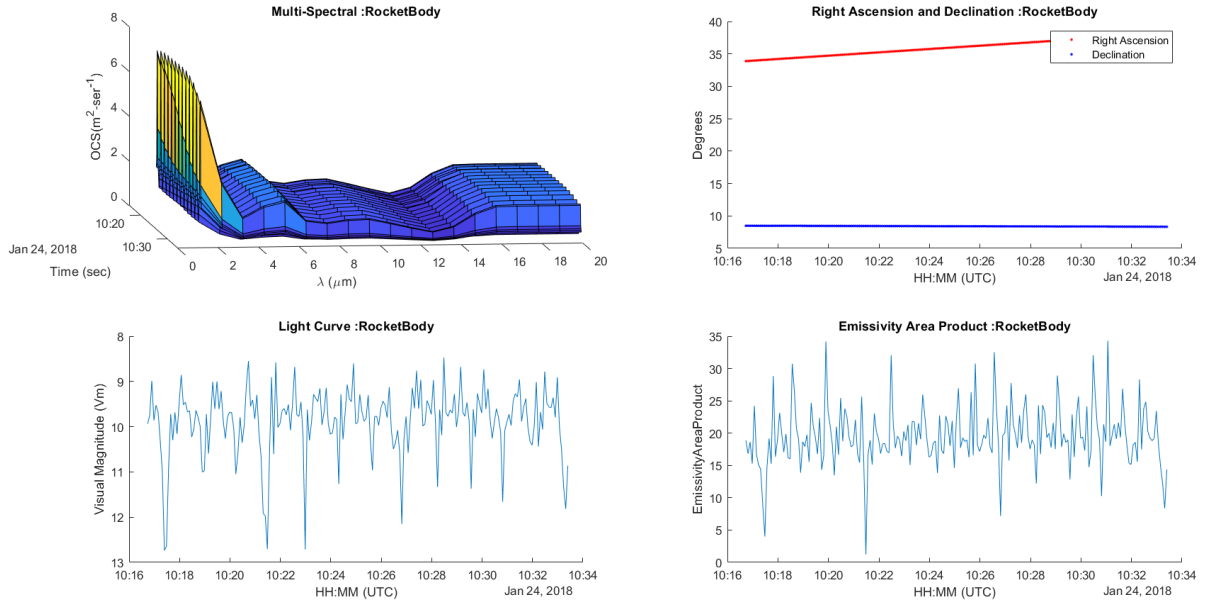


Figure 8. Simulated Measurements : Rocket Body

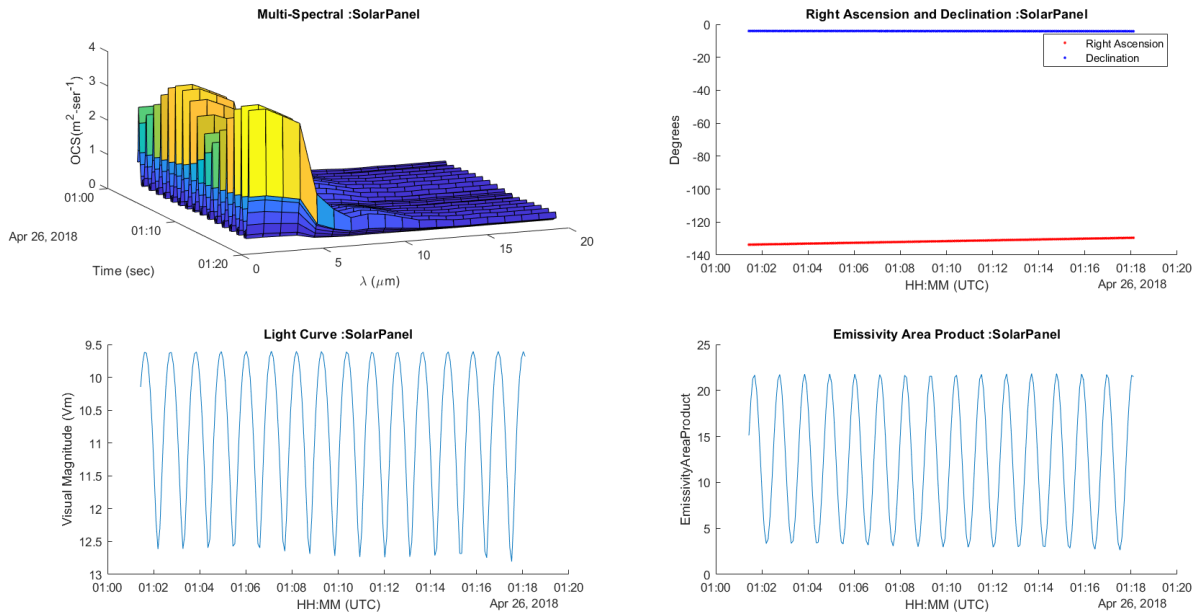


Figure 9. Simulated Measurements : Solar Panel

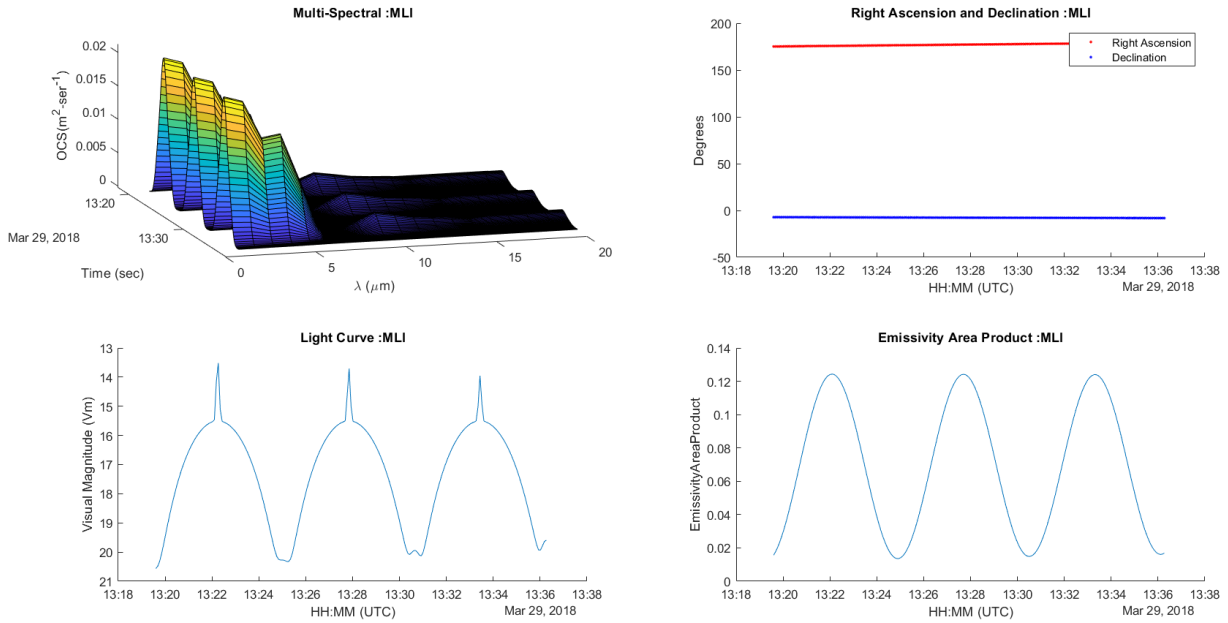


Figure 10. Simulated Measurements : Multi-Layer Insulation

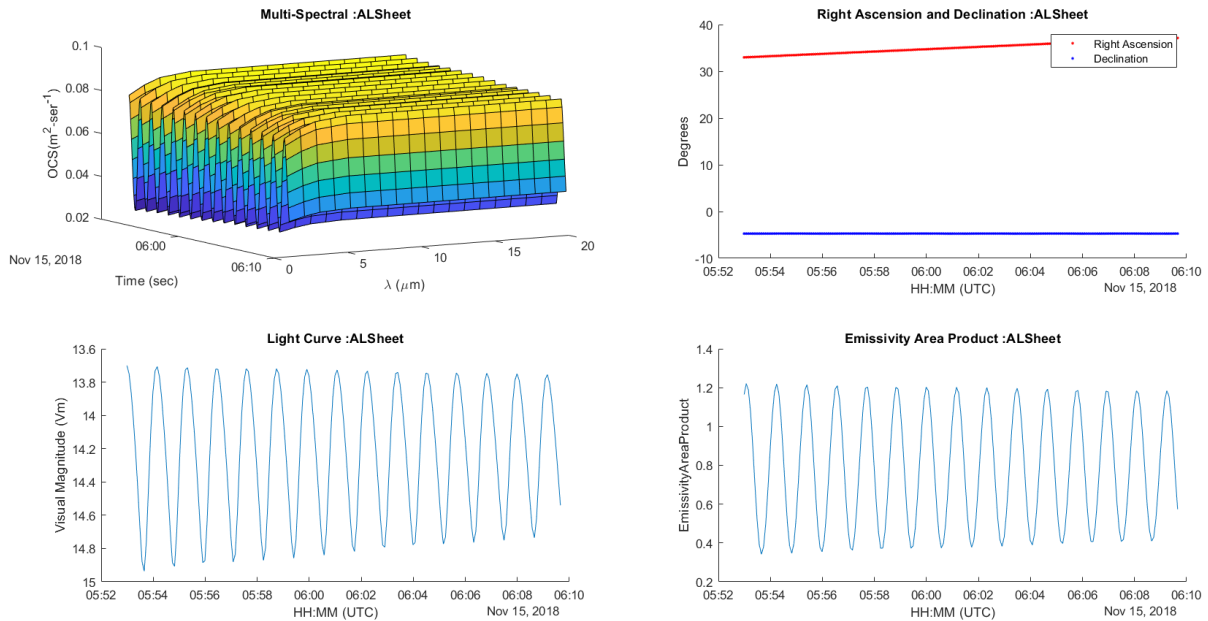


Figure 11. Simulated Measurements : Aluminum Sheet

As the six debris objects illustrate, each measurement type can be represented by a time history of observations consisting of a characteristic signature combined with both systematic and random errors resulting from imperfections intrinsic to the observing system, environment, and geometry. The signature itself is of interest as its variations over time and geometry reveal the physical and dynamic attributes of the unresolved object. In the next section of this paper an alternative representation of the multi-spectral measurements that is more conducive to exploring the information content is presented and provides an analytical tool for associating independent set of observations with no *a priori* association knowledge. The simulated test data sets are used to test these information-based techniques to show they can appropriately classify like attributes as well as provide indicators that selected light curve comparisons form different debris objects.

## 4. APPLICATION AND ANALYSIS OF CHARACTERIZATION TECHNIQUES

### 4.1. Mathematical and Probabilistic Motivation

This section presents techniques for extracting information used for characterization. A measurement time history can be mathematically represented as functions in order to use information theory to provide a rigorous probabilistic analysis of measurement phenomena. In the case of multi-spectral measurements, the time history is optical cross section (OCS) vs. time for a specified wavelength. The approach chosen differs from the conventional approach that treats measurements as a point-wise time series sequence of points. A measurement at time  $t$  over a time interval of length  $T$  is denoted by  $Z_t^T$ , object characteristic parameters by  $x_t$ , and geometric parameters by  $g_t$ . Only  $Z$  is treated as a curve (or model) over the interval  $T$ , while the state and geometric parameters are assumed to be represented in a holistic way based on the state of the object and geometric parameters over the window of time  $T$ . For example, the state  $x$  could represent the spin state of the satellite over the interval  $T$ , including the possibility that it is executing a complex attitude motion. A joint distribution on these parameters is denoted by  $p(Z_t, x_t, g_t)$  (for ease of notation, the superscript  $T$  is dropped). Along with the joint distribution, data models (e.g. wavelength dependent BRDF model for OCS) are used to compute the likelihood  $p(Z_t|x_t, g_t)$ . This same approach was used in a pointwise (i.e., not as a function) context of Multiple Model Adaptive Estimation (MMAE) in [2]. The probabilistic framework utilized in this work enables a rigorous Bayesian analysis, where the posterior characteristic associated with the object state can be computed given the observation and geometry parameters  $p(x_t|Z_t, g_t)$  or the joint posterior in both object state and geometric parameters given an observation  $p(x_t, g_t|Z_t)$ . This treatment, originally applied to a single measurement type, can be expanded to include multiple but independent measurement types such as for a multi-spectral sensor.

To probabilistically analyze multiple sets of measurement time series, tools from Functional Data Analysis (FDA) [8, 9] are used. Such an approach has been used in genetic analysis [10] and star and planetary classification based on an FDA analysis of light curves [11]. In fact, this work expands on Kelecy et al. [1] which demonstrated the use of FDA for characterizing states using light curves. In FDA, a curve is converted into a finite-dimensional vector using an appropriate basis system that guarantees capturing of the main features of a light curve signal. In general, the functional representation can be expanded to multiple dimensions to accommodate multiple independent measurement types. From there on, any result that is established for finite dimensional spaces can now be applied to multi-dimensional functional data. Reference [12] uses the Mahalanobis distance to process functional data for classification.

In addition to a rigorous Bayesian approach to light curve analysis, information theory can address many space domain awareness (SDA) problems. One can compute information divergence between two classes of multi-spectral data to assess how much common information exists between the two sets of data. Such an analysis can reveal, for example, that two objects share one or more common facets. Another example is to use mutual information to solve the object-to-object correlation problem by assessing how much information overlaps between two observed objects with two light curves collected at different time instances. The proposed FDA-based probabilistic viewpoint enables the replication of many of the information theoretic results developed for angles and/or range observations [13, 14] for light curves processing.

If one defines a “measurement state”  $x(t)$  as a function of time  $t$ , then for measurements of type  $z$  one can define  $n$  sets of measurements  $M_z$  over a sequence of  $m$  time-tags as

$$M_z = \{x_i(t_{ij}) : i = 1, \dots, n \text{ and } j = 1, \dots, m\} \quad (6)$$

where  $x_i(t_{ij})$  is a measurement in set  $i$  at the time instant  $j$ . It is also implied that, for multi-spectral data, there is a wavelength attribute that distinguishes the measurement. If one assumes that the measurements can be represented by a linear functional form in terms of basis functions  $\varphi_k(t_{ij})$  and coefficients,  $\beta_{ik}$  then

$$x_i(t_{ij}) \cong \sum_{k=1}^K \beta_{ik} \varphi_k(t_{ij}) \quad (7)$$

where  $K$  is the number of basis functions that adequately represent the measurements. The functional sample mean and covariance for the collection of measurements for a given type are then computed as

$$\hat{\mu}_x = \frac{1}{n} \sum_{i=1}^n \beta_i (t_{ij}) \quad (8)$$

and

$$\hat{\Gamma}_x = \frac{1}{n} \sum_{i=1}^n (\beta_i - \hat{\mu}_x)^T (\beta_i - \hat{\mu}_x) \quad (9)$$

It should be noted that the functional formulation removes the time-dependence and instead captures the statistical characteristics represented by the functional parameters  $\beta_{ik}$ . The previous work [1] showed the potential for ambiguous characterization results due to geometric and dynamic conditions that resulted in similar light curve characteristics. For example, a cube spinning about an axis that is aligned with the observer might look like a 3-axis stabilized cube, though the reflected light from the surface of the spinning cube does not vary with time as would be the case for the 3-axis stabilized cube. The value of multiple measurement types is the potential for providing additional information associated with different physical attributes that the ambiguous measurements do not provide.

#### 4.2. Computing Likelihood of a Measurement Phenomenon

Use of this “distance metric” is justified in terms of information similarities (or dissimilarities) by virtue of how closely the distributions between two classes of distributions compare. It is really the essence of the approach that is demonstrated in the simulated cases presented in the following section. The approach does not attempt to compare specific dynamic and physical attributes, but the statistical distributions associated with them. The implementation of this approach is, essentially, a hypothesis-based approach as one “hypothesizes” similarities (or dissimilarities) between distributions associated with the reference vs. test samples from which the statistics are derived.

The next question addressed in this paper is: How can one determine the likelihood that a measurement time history was generated by an debris object previously characterized (or classified)? Given a candidate object’s dynamics, shape type, and materials attributes the type’s first and second moment statistics are obtained as described in the last subsection. In the case of multi-spectral this would include spectral attributes based on material types (or combinations of materials for a non-homogeneous object). Those results suggest that the Mahalanobis type of distance metric can be used to assess whether the measurement sequence belongs to one of the available measurement classes [15]. This analysis enables the determination of whether a new measurement sequence belongs to a specific family of measurements associated with a specific class of object. It shows commonality of features between the new measurement sequence and ones in the family. These results also enable use of the divergence metrics, for example, to determine the degree of commonality between two classes of measurement populations. For this work, the use of a normalized distance metric is introduced which enables the combination of multiple distance measurements for each measurement type (e.g. OCS at a measured wavelength): The Hellinger Distance which is related to the Bhattacharyya divergence [15]. The Bhattacharyya divergence between two probability distribution functions (pdfs)  $p(x)$  and  $q(x)$  is given by:

$$D_B(p||q) = -\log(B_c(p||q)) \quad (10)$$

where  $B_c$  is the Bhattacharyya coefficient and is given by

$$B_c(p||q) = \int \sqrt{p(x)q(x)} dx \quad (11)$$

Note that  $0 \leq B_c(p||q) \leq 1$  and  $0 \leq D_B(p||q) \leq \infty$ , and so does not obey the triangle inequality. If both  $p$  and  $q$  are assumed to be Gaussian, then one can compute  $D_B(p||q)$  in closed form which is derived as:

$$D_B(p||q) = \frac{1}{8} (\mu_p - \mu_q)^T \Gamma^{-1} (\mu_p - \mu_q) + \frac{1}{2} \log \left( \frac{\|\Gamma\|}{\sqrt{\|\Gamma_p\| \|\Gamma_q\|}} \right) \quad (12)$$

where  $\mu_p$  and  $\Sigma_p$ , and  $\mu_q$  and  $\Sigma_q$ , are the mean and covariance of the distributions  $p$  and  $q$ ,  $\|\cdot\|$  denotes the determinant of the given covariance, and

$$\Gamma = \frac{1}{2}(\Gamma_p + \Gamma_q) \quad (13)$$

The Bhattacharyya coefficient is related to the Hellinger distance  $D_H$  as:

$$D_H(p||q) = \sqrt{1 - B_c(p||q)} \quad (14)$$

where  $D_B(p||q)$  is derived from equation (7) (assuming Gaussian distributions) and

$$B_c(p||q) = e^{-D_B(p||q)} \quad (15)$$

The Hellinger distance is a proper divergence metric because it satisfies the non-negativity, symmetry, and triangle inequality properties. This metric is used in the subsequent analysis to determine the “compatibility” of distributions of a set of one or more measurement types on a given debris object with the distribution metrics derived for an object with established distribution characteristics for those same measurement types. It is a measure of how one probability distribution is different from a second, reference probability distribution, where a divergence of 0 indicates that the two distributions in question are identical and at the opposite extreme a value of 1 indicates they are substantially different. If  $D_H^j(p_j||q_j)$  represents the Hellinger Distance between distributions  $p_j$  and  $q_j$  for measurement types  $j = 1, 2, \dots, N$ , then when considering the compatibility of distributions associated with multiple measurement types the combined distance metric can be computed by the Root Mean Square (RMS) as

$$D_H = \sqrt{\sum_{j=1}^N [D_H^j(p_j||q_j)]^2} / N \quad (16)$$

Though other means of combining the normalized distance metrics could be considered (e.g. weighted sum), the *RMS* was chosen for its simplicity but assumes equally weighted preference. This fusion of the Hellinger Distance metric for various combinations of measurements represents a combined likelihood of a given “test” measurement set being associated with a previously established set of statistics “trained” on a pre-established set of labelled data representing a state class. A value of  $D_H$  closer to zero indicates a close (“good”) comparison between distributions whereas a value closer to one indicates dissimilar (“poor”) comparison.

Use of this “distance metric” is justified in terms of information similarities (or dissimilarities) by virtue of how closely the distributions between two classes of distributions compare. It is really the essence of the approach that is demonstrated in the simulated cases presented in the following section. The approach does not attempt to compare specific dynamic and physical attributes, but the statistical distributions associated with them. The implementation of this approach is, essentially, a hypothesis-based approach as one “hypothesizes” similarities (or dissimilarities) between distributions associated with the reference vs. test samples from which the statistics are derived.

## 5. INFORMATION ASSESSMENT VS. MEASUREMENT COMBINATIONS

The simulated data was broken into two separate data sets, one as a reference set and the other for testing. For the multi-spectral measurements, each wavelength was treated as its own measurement set for characterization. First, we looked at a polynomial classification technique of the data with an initial rotation rate. In order to pick the best polynomial coefficient, multiple analysis runs were completed to determine which number of polynomial coefficient fits would provide the best results. The best polynomial coefficient found was 10 for the rotation. Below are the RMS of the 20 wavelength characterizations for the 6 debris objects with the reference data compared against the characterizations of the testing data.

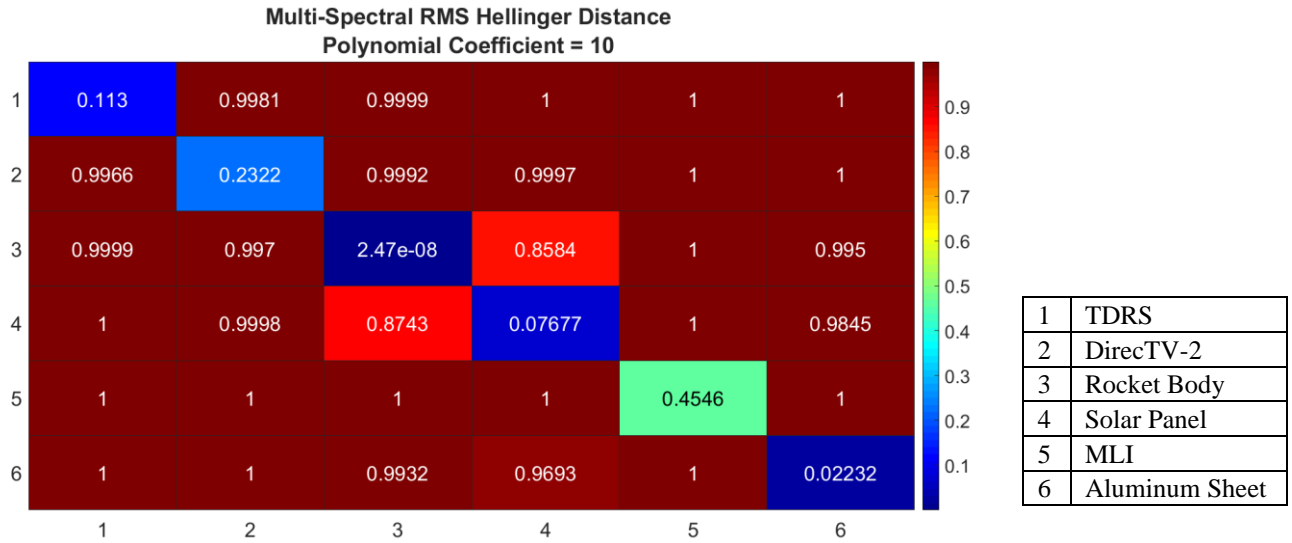


*Figure 12. Multi-Spectral RMS Hellinger Distance, Polynomial Coefficient = 10*

The RMS of the Hellinger Distances for the multi-spectral measurements across a spectrum of wavelengths characterized with a polynomial fit gives unambiguous characterization results. Comparisons of the TDRS, DirecTV-2, and Aluminum Sheet fingerprint with other debris all objects compare poorly (Hellinger Distance close to 1). The rocket body and solar panel compare well with themselves and most other debris objects, but do have a very small amount of ambiguity between each other. The MLI does not compare as well as expected with itself, this is due to the variation in the individual signatures. The variations do not match well with the other objects, but they do have trouble comparing with themselves in a statistical sense. With using a polynomial order of 10, the analysis polynomial coefficients that represented each data set and combined them to a mean over the reference and testing data sets. The coefficients were used in a polyval function to compare the statistical representation back to the simulated data. Unfortunately, the polynomial fit to the data did not translate well back to the simulated data. The FDA was able to find valuable information in the coefficient values, but they did not have a meaningful real data representation of the measurements. The coefficients represented a mean of the data and a some of the variation from the mean but does not physically represent the data very well. This was a major issue in assessing real data, addressed later in this paper, and led to investigating other methods for analyzing the measurements.

Next, we look at the same reference and testing data sets for the rotating debris objects, but instead of a polynomial fit, a Fast Fourier Transform was used to pull out the dominant frequencies in the data and evaluate them in a statistical framework. As the number of frequencies evaluated increased, the RMS Hellinger distances improved. Shown is where 25 frequencies were extracted from each set of simulated measurements.

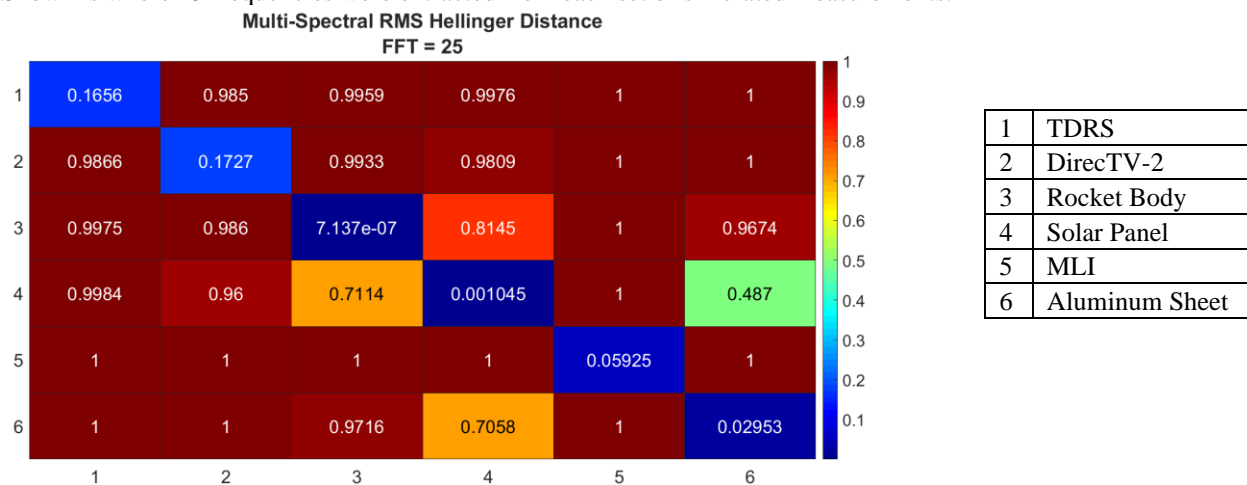


*Figure 13. Multi-Spectral RMS Hellinger Distance, FFT = 25*

With using the FFT analysis, the results did not provide as statistically convincing RMS Hellinger distances for unambiguous debris object characterization. In general, using FFT, there are still good comparisons between the same object, but more ambiguities across other debris object in some cases. More than a few of the dominant frequencies would not have any physical meaning but would represent noise that is in the measurements. The results indicate there is a statistical significance for the characterization of the frequencies that are representing the noise of the measurements. This result led to generating data without an initial rotation rate, to reduce the dominant frequencies extracted using the FFT method. This way, when the frequencies are analyzed they are based of the variations in the multi-spectral measurements and not due to the dynamics of the object.

Using the FFT analysis for the simulated debris objects without any initial rotation led to better RMS Hellinger distance values at lower frequencies. This result makes sense since the dominant frequencies of the rotating data, was in fact the rotation of the object. However, this did lead to ambiguities and worse statistical comparisons than the rotating case. Below the results are shown for FFT = 4 and FFT = 8.

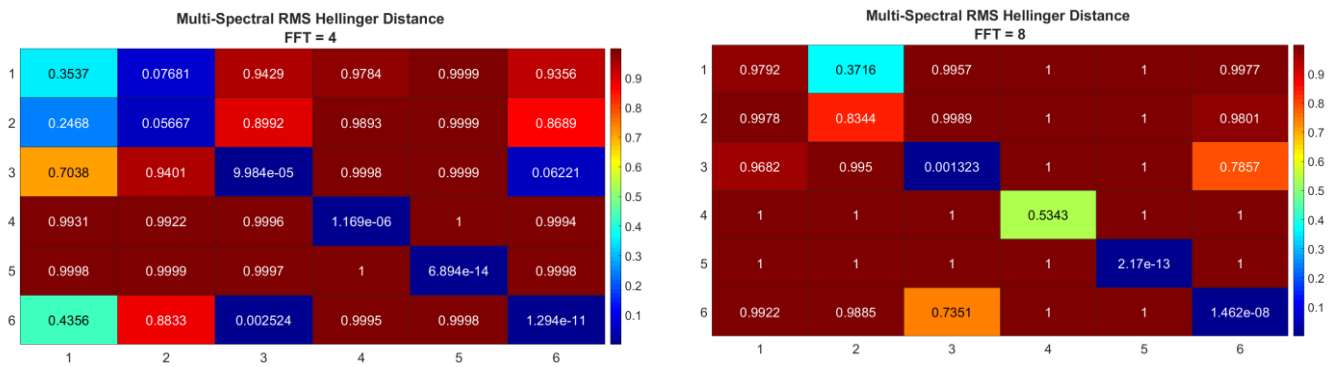
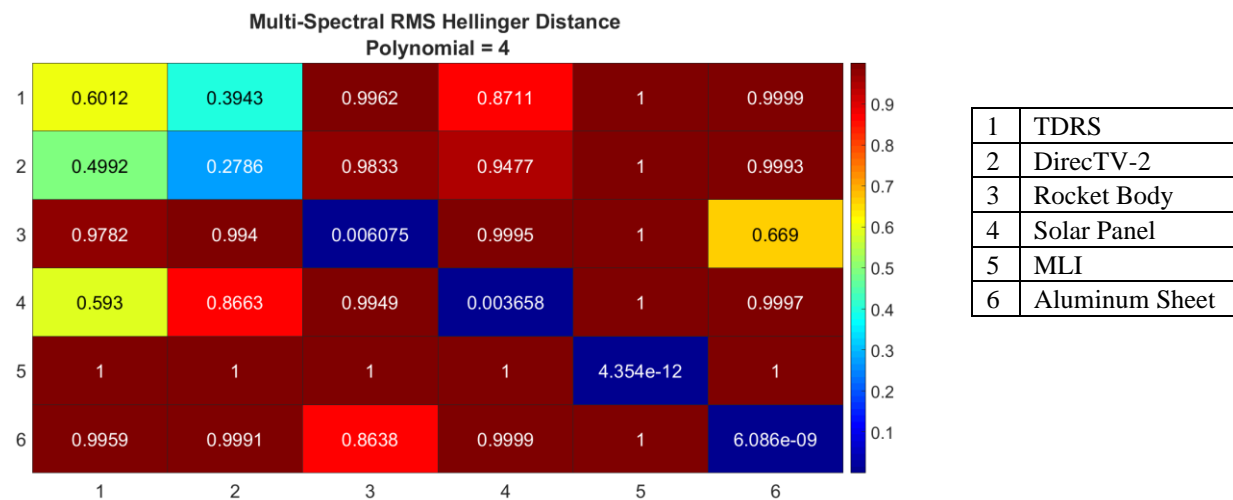


Figure 14. Multi-Spectral RMS Hellinger Distance, FFT = 4 and 8

Using FFT on non-rotating objects for characterization does not allow for unambiguous characterization, even using different frequency values. This shows that the TDRS, DirecTV-2, and Aluminum Sheet have trouble when comparing to other objects, and sometimes even when comparing to themselves when pulling out more frequencies. This could indicate the need for additional measurements to be included, like photometry to help distinguish the debris objects.

Additionally, the same polynomial analysis was repeated on the non-rotating debris objects. For the characterization, the fit was not done versus time, due to the small variation in time of the non-rotating object but done with respect to wavelength. The polynomial order fit was 4.



|   |                |
|---|----------------|
| 1 | TDRS           |
| 2 | DirecTV-2      |
| 3 | Rocket Body    |
| 4 | Solar Panel    |
| 5 | MLI            |
| 6 | Aluminum Sheet |

Figure 15. Multi-Spectral RMS Hellinger Distance, Polynomial = 4

The results show again an ability to classify certain debris objects, but not have unambiguous results. It does make sense that the TDRS, DirecTV-2 and Solar Panel have the potential to have similar characteristics due to the physical characteristics of the object. These simulated results point to some challenges that could be faced when applying to real data.

Lastly, it should be noted that this approach does require a “history” (e.g. library) of data on known and similar classes of objects. These are the “Reference” data sets that the “Test” data were compared against. How well dynamic and physical attributes of one state compare to the other states is virtually tested through the off diagonals of the characterization matrices which essentially compare what would be “class” not associated with the given test cases. If a class with dynamic and physical attributes not in line with the four states that were examined, then one would anticipate ambiguous (at best) or poor Hellinger metrics in some cases.

## 6. ANALYSIS ASSESSMENT ON REAL PHOTOMETRIC DATA

A sample of real data of Imarsat 3-F5 can be seen in the figure below.

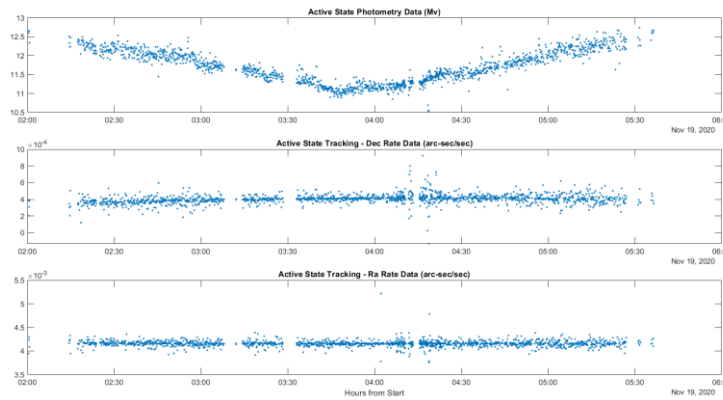


Figure 16. Imarsat 3-F5 Real Measurements

As shown in Figure 16, there is a relatively well behaved light curve, Dec Rate, and RA Rate data.

A sample of real data on DirecTV 1R can be seen in the figure below.

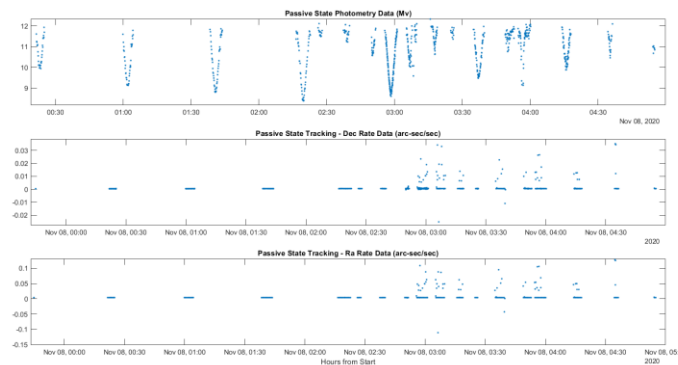


Figure 17. DirecTV 1R Real Measurements

As shown in Figure 17, the light curve is more sporadic and there is a lot of noise in the RA/Dec rates. The figure shows the raw data, which still has noise values included. The noise was removed for the analysis.

In the previous work with simulated data, measurement noise was added, but can be more accurately taken into consideration with the real data. Additionally, gaps in the data were not modelled, but are present in the real data and can affect the different types of analysis.

### FDA Polynomial Analysis Results

For the polynomial coefficient estimation, the first step was to take the training set of data and compute the coefficients and find the average of those coefficients. The results of average coefficient estimates can be seen in the following table :

Table 1 Polynomial Coefficient Means

|                         | Coefficient 1 |         | Coefficient 2 |         | Coefficient 3 |         |
|-------------------------|---------------|---------|---------------|---------|---------------|---------|
|                         | Active        | Passive | Active        | Passive | Active        | Passive |
| <b>Visual Magnitude</b> | 0.371         | 0.064   | 0.0039        | 0.0646  | 11.285        | 10.773  |
| <b>Dec Rate</b>         | 0.0004        | 0.0009  |               |         |               |         |
| <b>RA Rate</b>          | 0.004         | -0.011  |               |         |               |         |

The mean coefficients show a difference in the active and passive cases, but in order to bring statistical significance to this difference, the Hellinger Distance is used. The heatmaps of the Hellinger Distance for the polynomial comparison can be seen below.

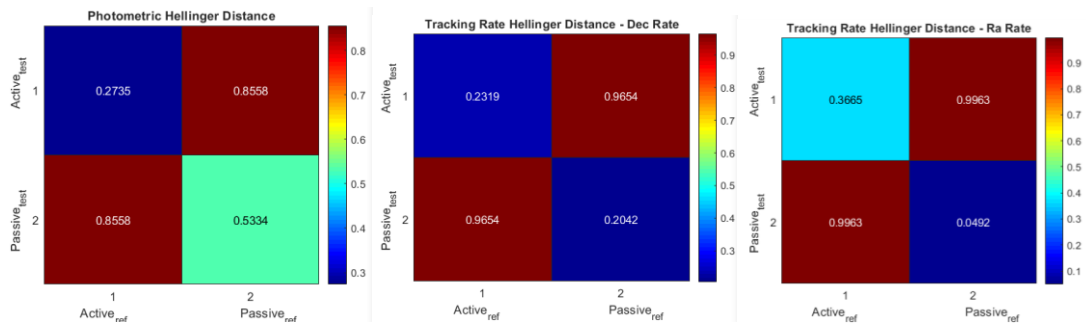


Figure 18. Polynomial Hellinger Distances

Figure 18 shows how well the analysis technique was able to characterize the data. An interesting result from this was the higher than expected Passive-Passive Hellinger Distance for photometry (0.5334). This is most likely due to the “randomness” associated with the real passive light curve that is harder to characterize. Fortunately, the other passive measurements were adequately characterized to still distinguish a passive RSO from an active RSO. The combined RMS of the Hellinger Distances can be seen in the table below:

Table 2 Polynomial RMS Hellinger Distances

|                                   | Active-Active | Active-Passive | Passive-Passive |
|-----------------------------------|---------------|----------------|-----------------|
| <b>RMS of Hellinger Distances</b> | 0.296         | 0.941          | 0.330           |

Table 2 shows the polynomial analysis is able to distinguish between active and passive satellites.

### FDA FFT Analysis Results

To estimate the mean max frequencies, the max frequencies were determined for the training sets and then averaged. The mean max frequencies can be found in the following table :

Table 3 FFT Mean Max Frequencies

|                         | Max Frequency 1 |         | Max Frequency 2 |         |
|-------------------------|-----------------|---------|-----------------|---------|
|                         | Active          | Passive | Active          | Passive |
| <b>Visual Magnitude</b> | 17174           | 6805    | 424             | 100     |
| <b>Dec Rate</b>         | 0.4794          | 1.3162  |                 |         |
| <b>RA Rate</b>          | 6.040           | 10.612  |                 |         |

Table 3 shows the mean max frequencies from the FFT Analysis. As expected there is a large difference in the visual magnitude max frequencies, the statistical significance of the differences can be seen in the following figure:

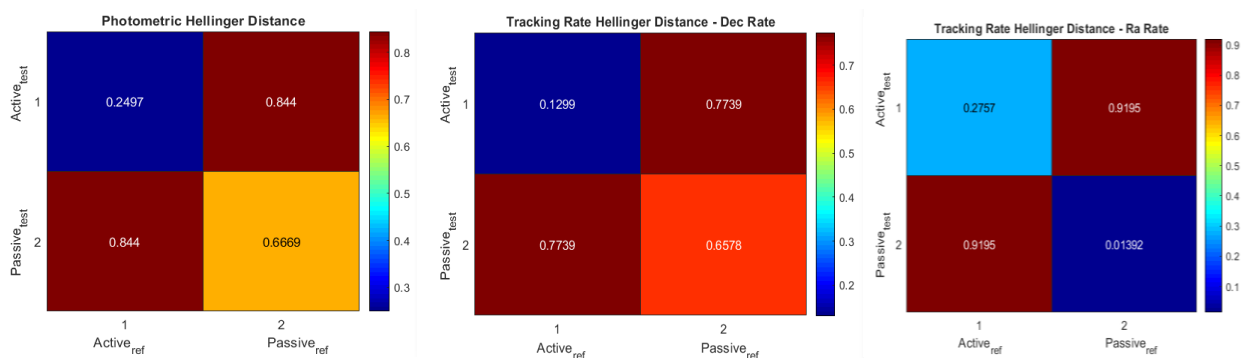


Figure 19. FFT Hellinger Distances

Similar to the polynomial case, the photometric passive-passive Hellinger Distance was more difficult to characterize. An unexpected result was the higher Hellinger Distance for the Dec Rate passive-passive case. This may be due to the noise and variability in the Dec Rate. This could be potentially alleviated in the future with larger training data sets that can better characterize the Dec Rate than can be compared to test states. Oppositely, the Ra Rate and visual magnitude are better characterized than in the polynomial analysis for the active-active cases.

The RMS Hellinger Distances can be seen in the following table:

Table 4 FFT RMS Hellinger Distance

|                                   | Active-Active | Active-Passive | Passive-Passive |
|-----------------------------------|---------------|----------------|-----------------|
| <b>RMS of Hellinger Distances</b> | 0.227         | 0.847          | 0.540           |

Table 4 shows the consistent ability to determine if the RSO is active, but has more difficulty in distinguishing between active-passive and determining if passive that the polynomial analysis.

For all cases, the worst Hellinger Distance was for the Passive-Passive Photometric comparisons. This is most likely due to the difficulty in characterizing a passive light curve and being able to generalize it enough to recognize another light curve as passive. For example, trying to fit a parabola to the light curve data shown in Figure 2 does not represent the data well. This is attempted to be overcome with the FFT analysis, but the difference in max frequencies between different real passive light curves is still large enough to manifest itself within the Hellinger Distance. With more training data samples, this problem should be addressed, but may not completely solve the problem of the difficulty in characterizing passive light curves.

## 7. CONCLUSIONS

This paper outlined the objective of being able to unambiguously classify different types of debris objects using just multi-spectral measurements. Reference and training data were generated in a Monte-Carlo like method for both rotating and non-rotating debris objects to be used in analysis. For the rotating data, the FDA was performed with polynomial coefficients (10) and FFT (25) that produced RMS Hellinger distances that allowed for unique classification of all of the debris objects presented. Next, the non-rotating objects used polynomial coefficients (4) and FFT (4) but were unable to produce unambiguous results. This could lead to difficulties in classifying debris objects with real multi-spectral data. With access to real photometric, the same analysis techniques were extended to real photometric data of an active and passive satellites. The results showed promise in being able to classify different types of RSO's but could need different analysis modes to produce the best results.

## 8. ACKNOWLEDGEMENTS

I would like to acknowledge the expert guidance and support for this paper from Dr. Thomas Kececy and thank L3Harris for their support in this research.

## 9. REFERENCES

1. Kececy, T., I. Hussein, K. Miller and J. Coughlin, "Probabilistic Analysis of Light Curves," Journal of the American Astronautical Society, ORCID ID 0000-0003-3958-6419, May 2018.
2. Linaris, R., Jah, M. K., Crassidis, J., Nebelecky, C.: Space Object Shape Characterization and Tracking Using Light Curve and Angles Data. Journal of Guidance Control and Dynamics, Vol. 37, No. 1, pp. 13-25, January (2014).
3. Kececy, T., E. Barker, P. Seitzer, T. Payne and R. Thurston, "Prediction and Tracking Analysis of a Class of High Area-to-mass Ratio Debris Objects in Geosynchronous Orbit," Proceedings from the 2008 AMOS Technical Conference, Wailea, Maui, HI, Sept 16-19, 2008.
4. Skinner, M., R. Russell, T. Kececy, S. Gregory, R. Rudy, D. Kim and K. Crawford, "Observations in the thermal IR and visible of a retired satellite in the graveyard orbit, and comparisons to active satellites in GEO," Acta Astronautica, 105 (2014) 1-10, Elsevier ScienceDirect, August 2014.
5. Skinner, M., R. Russel, T. Kececy, S/ Gregory, R. Rudy and D. Kim, "Comparison of Thermal IR and Visible Signatures of Graveyard Orbit Objects," 66<sup>th</sup> International Astronautical Congress, (IAC-15-A6.1.4) Jerusalem Israel, 2015.
6. Skinner, M., R. Russell, R. Rudy and D. Kim, "Broadband Array Spectrograph System (BASS) thermal IR observations of Low Earth Orbit (LEO) and Geosynchronous Earth Orbit (GEO) objects in sunlit and darkness conditions," 68<sup>th</sup> International Astronautical Congress, (IAC-17-A6.1.6) Adelaide, Australia, 2017.
7. Skinner, M., R. Russell, R. Rudy and D. Kim, "Utilization of Broadband Array Spectrograph System (BASS) thermal IR observations of geosynchronous earth orbit (GEO) objects in the creation of an observation-based model of their thermal emission," 69<sup>th</sup> International Astronautical Congress, (IAC-18-A6.1.5) Bremen, Germany, 2018.
8. Gine, E., Nickl, R.: Mathematical Foundations of Infinite-Dimensional Statistical Models. Cambridge Series in Statistical and Probabilistic Mathematics (2015).
9. Wang, J. L., Chiou, J. M., Muller, H. G.: Review of functional data analysis. Annual Review of Statistics and Its Application, Vol. 3, pp 257-295 (2016).
10. Leng, X., Müller, H. G.: Classification using functional data analysis for temporal gene expression data. Bioinformatics, 22 (1): 68-76 (2006).
11. Faraway J., Mahabal, A., Sun, J., Wang, X.-F., Wang, Y. G., Zhang, L.: Modeling light curves for improved classification of astronomical objects. Statistical Analysis and Data Mining, Vol. 9, pp. 1-11 (2016).
12. Galeano, P., Joseph, E., Lillo, R. E.: The Mahalanobis Distance for Functional Data with Applications to Classification. Technometrics, Vol. 57, No. 2, pp. 281-291 (2015).
13. Hussein, I., Wilkins, M. P., Roscoe, C. W. T., Schumacher, Jr., P. W.: On Mutual Information for Observation-to-Observation Association. 25<sup>th</sup> AAS/AIAA Space Flight Mechanics Meeting, Williamsburg, VA, January 11-15 (2015).
14. Hussein, I., Roscoe, C. W. T., Schumacher, Jr., P. W., Wilkins, M. P.: UCT Correlation using the Bhattacharyya Divergence. Proceedings of the 26<sup>th</sup> AAS/AIAA Space Flight Mechanics Meeting, Napa, CA, February 14-18 (2016).
15. Hussein, I., C. Roscoe, M. Wilkins and P. Schumacher, "Track-to-Track Association Using Bhattacharyya Divergence," Proceedings of the 16<sup>th</sup> AMOS Technical Conference, Wailea, HI, 2015.
16. Hall, D. K. Hamada, T. Kececy and P. Kervin, "Surface Characterization from Non-resolved Multi-band Optical Observations," Proceedings of the 13<sup>th</sup> AMOS Technical Conference, Wailea, HI, 2012.

17. Hall, D, B. Calef, K. Knox, M. Bolden and P. Kervin, "Separating Attitude and Shape Effects for Non-Resolvable Objects," Proceedings of the 8<sup>th</sup> AMOS Technical Conference, Wailea, HI, 2007.